

# Large Eddy Simulation of Turbulent Flow Over Fluid-Saturated Porous Media

# LARGE EDDY SIMULATION OF TURBULENT HEAT AND FLOW OVER FLUID-SATURATED POROUS MEDIA

**Mohammad Jadidi*, Yasser Mahmoudi**

Department of Mechanical, Aerospace and Civil Engineering, University of Manchester, Manchester M13 9PL, United Kingdom

## ABSTRACT

In this paper, the heat and fluid flow behaviour for a channel partially filled with two different porous blocks and a solid block is investigated numerically using a detailed pore-scale large eddy simulation (LES). Results show that a significant portion of the fluid entering the porous blocks leaks from the porous region to the non-porous region through the porous-fluid interface. Detailed flow patterns visualization inside the porous blocks indicate that the flow leakage leads to the creation of counter-rotating vortex pairs of fluid flow within and above the porous blocks that result in the formation of organized hairpin structures. Investigation of coherent structures show that the legs and the head of hairpins are generated separately by different mechanisms; the legs are produced by flow leakage while the heads are created by vorticity rollup at the shear layer above the porous interface. Finally, results show that the heat transfer mechanisms over the porous media are governed by the formation of organized hairpin structures.

## 1. INTRODUCTION

The exchange of heat and flow between the porous and non-porous regions is gaining expanding academic and industrial attention [1-4]. Despite the clear relevance and importance of composite porous-fluid systems to a wide range of applications, the problem of fluid flow and heat transfer in such systems have not been fully resolved. This study aims to use large eddy simulations (LES) to obtain new information on the fluid flow and heat transfer between the porous and non-porous regions and to address the connection between these two regions. The findings of this study are insightful for the community in this field to develop proper momentum and thermal boundary conditions at the porous-fluid interface which has been a challenging question for more than four decades [6-8].

## 2. COMPUTATIONAL METHODOLOGY

The computational domain is a channel partially filled with two different porous structures and a solid block depicted in Figure 1. The first porous block is a packed bed made of spheres with a diameter of D and the second one is formed from a rectangular cross-section ligament with a thickness of 0.26D. The blockage ratio (i.e., the ratio of the height of the porous region to the channel height) is 0.5 in all cases. The computational domain has the dimensions of 70D, 6D, and 5D in the x, y, and z directions, respectively. The Reynolds number (based on the channel hydraulic diameter and inlet velocity ($U$)) is 3300. The details of boundary conditions are depicted in Figure 1(c).

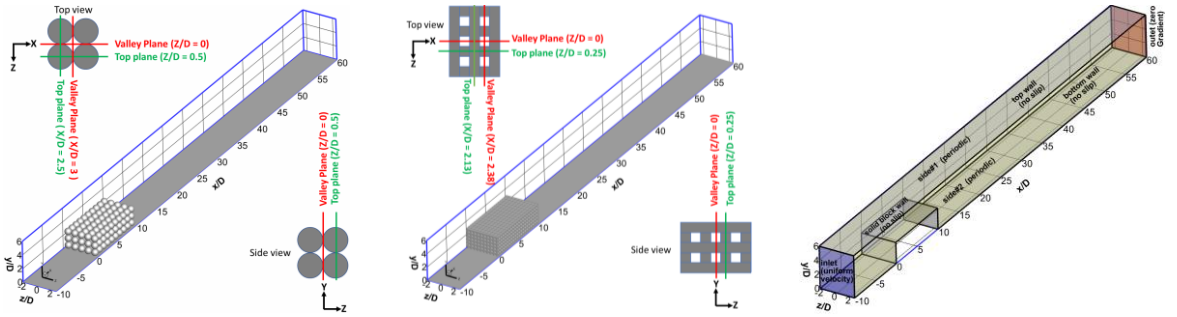


**a.** Structure A **b.** Structure B **c.** Structure C

*Corresponding Author: mohammad.jadidi@manchester.ac.uk

**Figure 1:** Computational domain; **a**: Porous structure with cubic packed arrangement formed from spheres (bridge method has been employed at the contact point of spheres, porosity 53%, D=6 mm); **b:** Porous structure formed from rectangular cross-section ligament (porosity 46.4%); **c:** Solid block; The red solid line lies over the valley plane and the green line lies over the top plane

Numerical simulation is based on the finite volume method, applying the unsteady PISO algorithm [9] and deploying 10.3 million non-uniform computational cells. The LES sub-grid scale (SGS) model is developed in OpenFOAM using the dynamic SGS turbulent kinetic energy model. To accurately capture the evolution of the flow features, the physical time step is chosen for each grid such that the CFL number is kept below unity. Time averaging process is begun when the initial transient conditions are washed out. All the present numerical results are averaged over a period of 490 non-dimensional time units ($t^* = t \times U/D$).

## 3. VALIDATION

The developed LES solver has been validated with respect to the experimental data of Leu, et al. [10]. They measured flow velocity components and turbulence statistics in a channel with a porous block mounted on the bottom wall. The porous block consisted of glass beads, having diameters (D = 0.015m that were arranged in a non-staggered pattern with a porosity of 47.5%. The length (L), width (W), and height (H) of the block are 0.15m, 0.3m and 0.075m, respectively. Figure 2 compares the present LES results and experimental data for streamwise and vertical velocity components, Reynolds shear stress and turbulent kinetic energy above the porous block at $X/H = 1.6$. The figure shows that the developed LES model can predict well the experimental data at locations above the porous block and in the wake downstream of the porous block. The slight discrepancy observed in Fig. 3 is attributed to the RANS input data employed for the LES inflow turbulence generation.

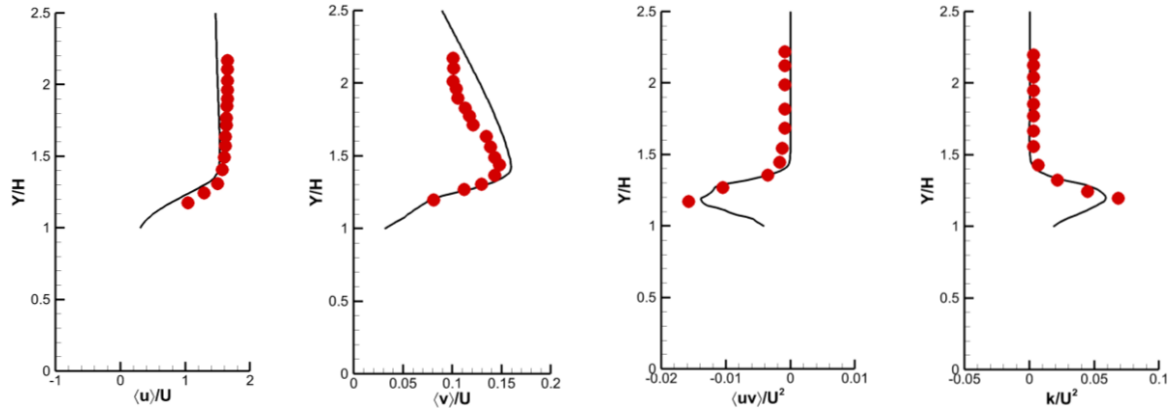


**a**) Streamwise velocity **b**) Vertical velocity **c**) Reynolds shear stress **d**) Turbulent kinetic energy

**Figure 2** Comparison of velocity profiles, Reynold shear stress $\langle u'v' \rangle / U^2$ and turbulent kinetic energy TKE $= 0.5 \left( \overline{u'^2} + \overline{v'^2} + \overline{w'^2} \right)$ obtained from the present LES study (solid lines), against the experimental measurements (symbols) of above the porous interface at $X/H = 1.6$

## 4. RESULTS AND DISCUSSION

Vertical velocity components and pressure distribution through and over the porous blocks have been demonstrated in Figure 3. It is seen that the flow features are nearly similar for both porous structures. Contours of vertical velocity and the streamlines in Figure 3 explain that some portion of the fluid entering the porous blocks is forced up toward the porous-fluid interface and leave the porous structures to the clear region (flow leakage). This phenomenon has been illustrated by the positive iso-surface of vertical velocity in Figure 3(d, h). These figures demonstrate that the boundary layer on the porous interface is changed by the flow leakage as will be discussed in Figure 6.

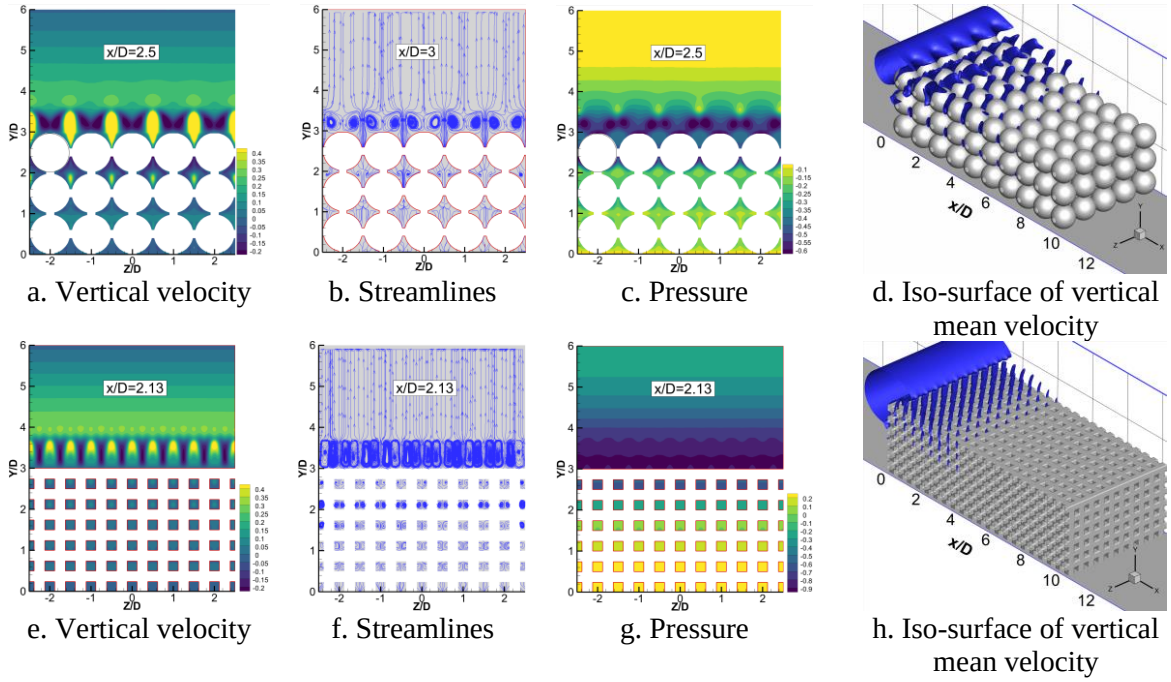


a. Vertical velocity b. Streamlines c. Pressure d. Iso-surface of vertical mean velocity

e. Vertical velocity f. Streamlines g. Pressure h. Iso-surface of vertical mean velocity

**Figure 3**: Side view contour plots of vertical velocity component($\langle v/U \rangle$), streamlines, pressure contour plots ($\langle p/\rho U^2 \rangle$) and three-dimensional representation of flow leakage from porous by iso-surface of vertical mean velocity ($\langle v/U \rangle = 0.5$); **Top:** Structure A**; Bottom:** Structure B

Figure 4 shows the contours of instantaneous and time-averaged temperature on the trough plane. It shows that after the flow impingement on the windward face of the porous blocks, the low-temperature flow penetrates the pores of the porous block and forms high momentum channelling in the porous region. Moreover, low-temperature flow leakage from the porous region into the non-porous region across the interface is clear on the trough planes.

The pattern of temperature below the interface confirms the modifications of the flow close to the interface; flow leakage from the porous region to the non-porous region clogs the horizontal channels near the interface. This observation shows the deterioration of low-temperature channelled flow in the upper layer of the porous blocks due to the flow leakage.

Above the porous-fluid interface in the non-porous region, the pattern of temperature shows the growth of the shear layer. The evolution of the shear layer is divided into three sections. The first one is characterised by the flow separation at the leading edge of the porous block. The second segment is identified by vortex formation and pairing that lead to the rapid growth of the shear layer. At this stage, spanwise vortex structures (rollers) are formed as illustrated in **Figure 5**. This marks the beginning of the second phase of the evolution of the shear layer. From the local up-inclined high-temperature regions in **Figure 5**(c), it can be seen clearly that there are upward-lifting motions of the vortices, which pumps the near-wall high-temperature fluids into the upper low-temperature stream. As shown in **Figure 5**(a-b), the rollers cannot extend into the porous medium due to the flow leakage from subsurface flow to the surface flow at the interface and the rollers lie above the interface. The third segment is characterised by cross interaction of wake and shear layer that leads to the deterioration of the rollers.

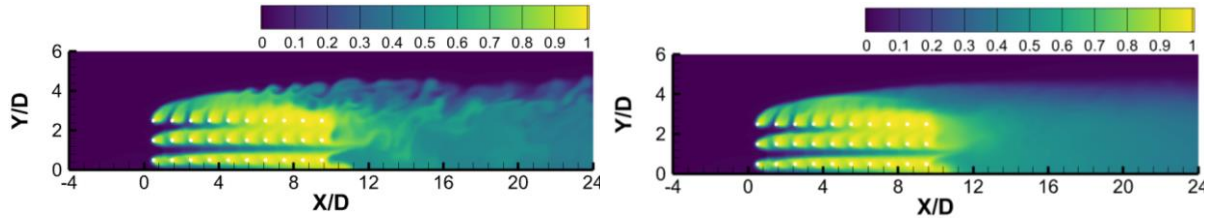


**a**) Instantaneous temperature **b**) Time-average temperature

**Figure 4** Contour of **Left**: instantaneous; and **Right**: time-averaged temperature on the trough plane

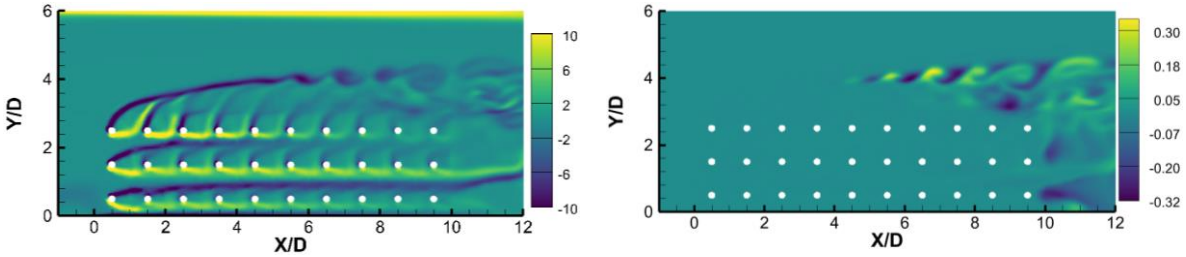


a) Representation of vorticity rollup by the contour of spanwise vorticity

b) Demonstration of vorticity rollup by the contour of temperature fluctuation

**Figure 5** Vorticity rollup at the shear layer above the interface in the non-porous region

Figure 6(a-c) show iso-surfaces of vortex strength that exhibit a forest of vortices with clear hairpin structure: a spanwise-oriented 'head' connected to counter-rotating quasi-streamwise 'legs. The flow patterns above the porous blocks are almost like those with the impermeable wall boundary layers in Figure 3 (c). [11] for impermeable wall reported that the vortex head (seen in Figure 6(d) and 3(e)) and the shear layer line corresponds to a hairpin vortex signature. However, for the solid block in Figure 6(c), the hairpin structures are not well-organised as can be observed for the porous structures; it is nearly difficult to visually detect distinctive flow patterns of vortex heads. Figure 6(g-h) show the sense of rotation of the legs of the hairpin structures that is consistent with the positive and negative streamwise vorticity above the porous interface demonstrated in Figure 3(b) and 2(f).

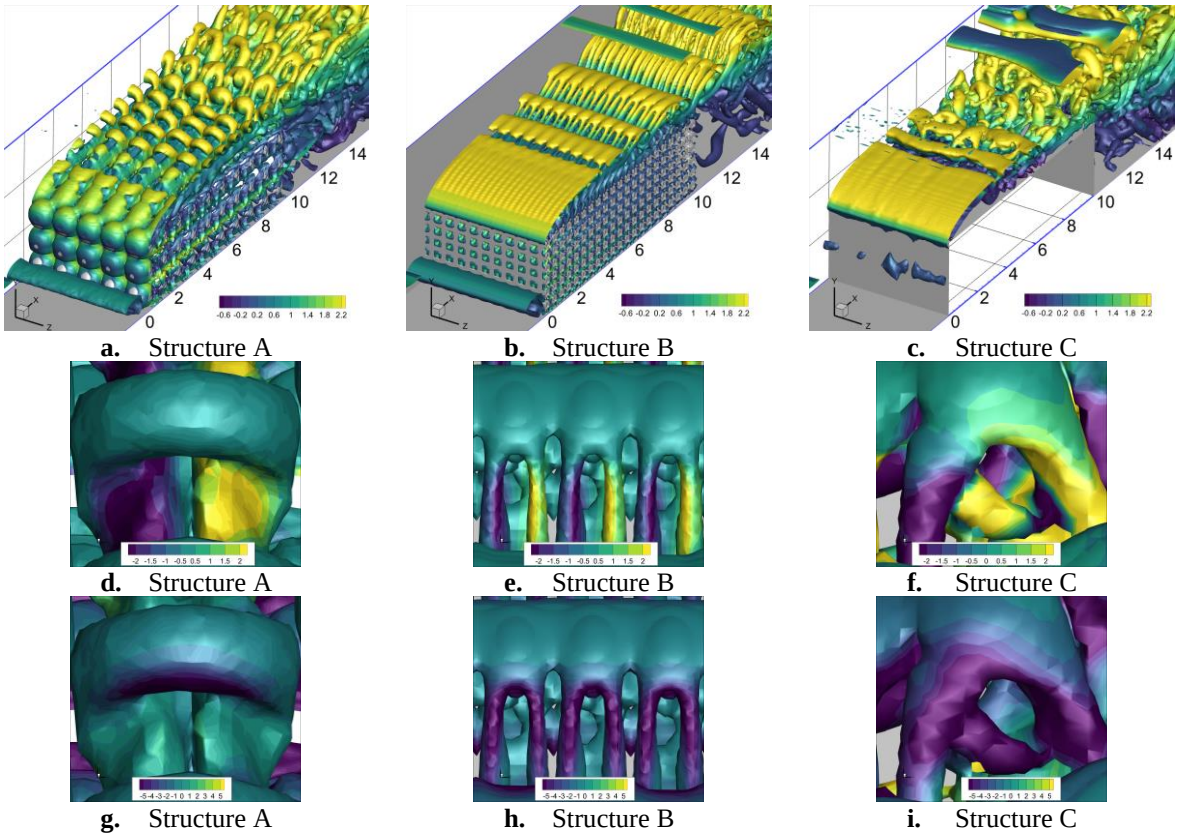

**a.** Structure A **b.** Structure B **c.** Structure C

**d.** Structure A **e.** Structure B **f.** Structure C

**g.** Structure A **h.** Structure B **i.** Structure C

**Figure 6**: Three-dimensional coherent structures identified by instantaneous iso-surface of $Q$-criterion ($Q = 2000s^{-2}$ ); **Top:** Coherent structures coloured by streamwise velocity ($\langle u/U \rangle$); **Middel:** Coherent structure coloured by streamwise vorticity ($\langle \omega_x D/U \rangle$); (close up view); **Bottom:** Coherent structure coloured by spanwise vorticity($\langle \omega_z D/U \rangle$); (close up view)

## 5. HEAT TRANSFER MECHANISM

The vortex line shows a pair of inclined counter-rotating quasi-streamwise vortices located on either side of the leg and neck of the hairpin in Figure 7(a). Streamlines show CRVP around counter-rotating quasi-streamwise vortices. The leg and neck rotation of the hairpin structure is consistent with the positive and negative streamwise vorticity induced by CVPs above the porous interface in Figure 6 and Figure 3.

Streamlines and vectors of vertical velocity fluctuations around the head of the hairpin in Figure 7(b) show the induced flow by clockwise rotation (negative spanwise vorticity) of the head of the hairpin. It shows how high-temperature fluid over the interface is pushed upward and the low-temperature fluid above the shear layers is drawn downward.

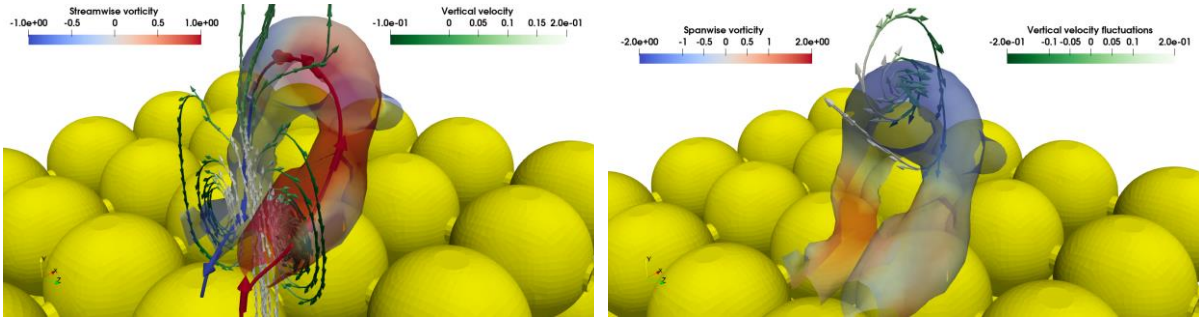


a) Hairpin legs and CRVP b) Hairpin head and spanwise vorticity

**Figure 7** Turbulent heat transfer mechanism over a porous block by a hairpin vortex; a: a hairpin structure coloured by streamwise vorticity; b: clockwise rotation of the head of the hairpin coloured by spanwise vorticity; vectors show induced fluid flow by instantaneous velocity fluctuations around the head of the hairpin

## 6. TURBULENCE STATISTICS

Vertical distributions of turbulent kinetic energy (TKE), $\langle k/U^2 \rangle$, through and over the porous block are compared with a solid block in Figure 8. For all three structures, the maximum values of TKE occur at the shear layer elevation above the porous-fluid interface (at the height of the head of the hairpins in Figure 6(g-i)); however, the absolute magnitudes of TKE are decreased drastically for the porous blocks. The main reason for the reduction of TKE for the porous block is that the reverse flow on the porous interface is deteriorated by flow leakage as compared with the strong reverse flow above the solid block.

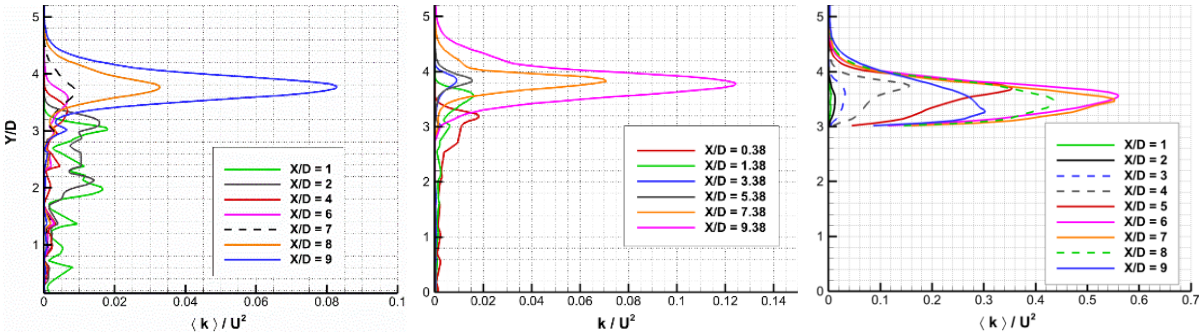


**a.** Structure A **b.** Structure B **c.** Structure C

**Figure 8**: Vertical distribution of turbulent kinetic energy ($\langle k/U^2 \rangle$) at different sreamwise locations

## 7. CONCLUSIONS

Pore-scale LES investigation has been conducted to better understand the flow features at the interface between a porous saturated media and a clear fluid above it. The primary observation in this work is that the fluid entering the porous blocks is pushed upwards toward the porous interface and

leaves the porous region. The leakage clogs the horizontal channels inside the porous block which induces a significant reduction in streamwise momentum of the pore flow near the interface. Moreover, the boundary layer over the porous-fluid interface is continuously disrupted by the flow leakage across the interface. Findings demonstrate the formation of organized counter-rotating vortex pairs (CRVPs) of fluid flow within and above the porous blocks due to the flow leakage. Flow visualization shows that the CRVPs originate from the bottom of the porous block and move upwards altering the coherent structures of the flow above the interface. The distribution of streamlines and vorticity components indicate that the rotation of the neck of the hairpin structures is consistent with the CRVPs above the porous interface. Whereas, the head of the hairpin is created by vorticity rollup at the shear layer above the porous interface. Finally, results indicate that heat transfer mechanisms over the porous interface is mainly controlled by CRVPs and hairpin vortex structures.

## ACKNOWLEDGEMENT

This work was supported by the UK Engineering and Physical Sciences Research Council (EPSRC) [grant numbers EP/T012242/1 and EP/T012242/2]. Data supporting this publication can be obtained on request. The authors would like to acknowledge the assistance given by Research IT and the use of the Computational Shared Facility at The University of Manchester.

## REFERENCES

[1] X. Chu, W. Wang, G. Yang, A. Terzis, R. Helmig, and B. Weigand, "Transport of Turbulence Across Permeable Interface in a Turbulent Channel Flow: Interface-Resolved Direct Numerical Simulation," *Transport in Porous Media,* vol. 136, no. 1, pp. 165-189, 2021-01-01 2021, doi: 10.1007/s11242-020-01506-w.

[2] Y. Kuwata and K. Suga, "Transport Mechanism of Interface Turbulence over Porous and Rough Walls," *Flow Turbulence and Combustion,* vol. 97, no. 4, pp. 1071-1093, 2016, doi: 10.1007/s10494-016-9759-9.

[3] A. Leonardi, D. Pokrajac, F. Roman, F. Zanello, and V. Armenio, "Surface and subsurface contributions to the build-up of forces on bed particles," *J. Fluid Mech.,* vol. 851, pp. 558-572, 2018-09-25 2018, doi: 10.1017/jfm.2018.522.

[4] F. Shikh Anuar, K. Hooman, M. R. Malayeri, and I. Ashtiani Abdi, "Experimental study of particulate fouling in partially filled channel with open-cell metal foam," *Experimental Thermal and Fluid Science,* vol. 110, p. 109941, 2020/01/01/ 2020, doi: https://doi.org/10.1016/j.expthermflusci.2019.109941.

[5] F. Shikh Anuar, I. Ashtiani Abdi, and K. Hooman, "Flow visualization study of partially filled channel with aluminium foam block," *International Journal of Heat and Mass Transfer,* vol. 127, pp. 1197-1211, 2018, doi: 10.1016/j.ijheatmasstransfer.2018.07.047.

[6] B. Alazmi and K. Vafai, "Analysis of fluid flow and heat transfer interfacial conditions between a porous medium and a fluid layer," *International Journal of Heat and Mass Transfer,* vol. 44, no. 9, pp. 1735-1749, 2001/05/01/ 2001, doi: https://doi.org/10.1016/S0017-9310(00)00217-9.

[7] Y. Mahmoudi, N. Karimi, and K. Mazaheri, "Analytical investigation of heat transfer enhancement in a channel partially filled with a porous material under local thermal non-equilibrium condition: Effects of different thermal boundary conditions at the porous-fluid interface," *International Journal of Heat and Mass Transfer,* vol. 70, pp. 875-891, 2014, doi: 10.1016/j.ijheatmasstransfer.2013.11.048.

[8] G. S. Beavers and D. D. Joseph, "Boundary conditions at a naturally permeable wall," *J. Fluid Mech.,* vol. 30, no. 1, pp. 197-207, 1967, doi: 10.1017/S0022112067001375.

[9] H. K. Versteeg and W. Malalasekera, *An Introduction to Computational Fluid Dynamics: the Finite Volume Method,* 2nd Edition ed. Harlow, England;: Pearson Education Limited., 2007.

[10] J. M. Leu, H. C. Chan, and M. S. Chu, "Comparison of turbulent flow over solid and porous structures mounted on the bottom of a rectangular channel," *Flow Measurement and Instrumentation,* vol. 19, no. 6, pp. 331-337, 2008/12/01/ 2008, doi: 10.1016/j.flowmeasinst.2008.05.001.

[11] R. J. Adrian, C. D. Meinhart, and C. D. Tomkins, "Vortex organization in the outer region of the turbulent boundary layer," *J. Fluid Mech.,* vol. 422, pp. 1-54, 2000, doi: 10.1017/S0022112000001580.